PAPER

Synthesis and dielectric properties of nanocrystalline oxide perovskites, $[KNbO_3]_{1-x}[BaNi_{0.5}Nb_{0.5}O_{3-\delta}]_x$, derived from potassium niobate $KNbO_3$ by gel collection†

Julien Lombardi,[abc] Frederick Pearsall,[abc] Wanlu Li[bc] and Stephen O'Brien*[abc]

Inorganic materials synthesis techniques that can approach low temperature routes akin to chemical solution processing are attractive for their ability to prepare nanocrystalline oxides. These methods can offer thin film integration options more compatible with modern device platforms such as spray coated or printed devices (2D, 3D) and flexible electronics. A chemical solution processing method based on sol–gel chemistry was used to obtain a set of perovskite compounds of the formula $[KNbO_3]_{1-x}[BaNi_{0.5}Nb_{0.5}O_{3-\delta}]_x$, called KBNNO, a class of visible light absorbing ferroelectric photovoltaic materials, with a tunable band-gap as a function of x. The materials produced were fully crystallized with average nanoparticle sizes of 15–20 nm (KNO) and 20 nm (KBNNO). Control over the composition of KBNNO was based on the synthesis of nanocrystalline potassium niobate $KNbO_3$ (KNO) *via* potassium and niobium ethoxides, with subsequent chemical reaction of complimentary barium and nickel alkoxides and methoxyethoxides. Characterization by Raman, TEM, SEM, XRD, and EDS confirms structure and composition. Following the introduction of Ba and Ni, a transition from the original orthorhombic *Amm*2 unit cell ($x = 0$) to a more complex atomic arrangement in cubic *Pm*3*m* ($x > 0.1$) is observed. This synthetic route to KBNNO, previously only synthesized by solid state processing at 1050–1200 °C, provides a lower temperature ($<$525 °C) approach to doping ferroelectric $KNbO_3$ with Ba and Ni, which inserts Ba^{2+} onto the A-site, and Ni^{2+} onto the B-site with the addition of oxygen vacancies for charge compensation. Frequency dependent dielectric measurements, performed on KNO–PFA (poly furfuryl alcohol) and KBNNO–PFA nanocomposites, show stable effective dielectric constants of 41.2, 70.8, 94.0, and 108.3 for KNO, KBNNO $x = 0.1$, 0.2, and 0.3 respectively at 1 MHz. Using full error analysis and the modified interphase model, a Maxwell-Garnett based micromechanics approach, the dielectric constant of the individual nanoparticles of KNO, KBNNO $x = 0.1$, $x = 0.2$, and $x = 0.3$ were calculated to be 154, 180, 225, and 255 respectively. The decrease in observed values relative to bulk films is attributed to a potential particle size suppression of the ferroelectric behavior.

[a] The CUNY Energy Institute, City University of New York, The City College of New York, Steinman Hall, 160 Convent Avenue, New York, NY 10031, USA. E-mail: sobrien@ccny.cuny.edu

[b] Department of Chemistry, The City College of New York, 1024 Marshak, 160 Convent Avenue, NY 10031, USA

[c] Ph.D. Program in Chemistry, The Graduate Center of the City University of New York, New York, New York, NY 10016, USA

† Electronic supplementary information (ESI) available. See DOI: 10.1039/c6tc02327d

Introduction

Of the perovskite class of ferroelectrics, potassium niobate ($KNbO_3$) is one of the most studied due to the range of interesting properties attainable.[1,2] $KNbO_3$ has a nonlinear optical response,[3] due to its spontaneous polarization at room temperature, as well as frequency doubling[4] in low and medium powered lasers. $KNbO_3$ is of particular interest to many scientists because of its high temperature ferroelectricity and piezoelectricity, useful for device functionality, with the added benefit of being lead free.[1,2] Furthermore, the possibility of doping the structure with elements allows for the properties to be further modified or tuned.[5–7] Traditional solid state methods to synthesize $KNbO_3$ use high temperatures in the range of 1100–1200 °C.

Recently the prospect of using perovskite oxides for visible-light-absorbing ferroelectric and photovoltaic materials has been reported, and KBNNO has gained attention for its performance as a ferroelectric photovoltaic.[8,9] The proposition is that the presence of strong inversion symmetry breaking from spontaneous electric polarization can promote the desirable separation of photo-excited carriers, allowing voltages above the bandgap, which may enable efficiencies beyond the maximum possible in

a conventional p–n junction solar cell. It has been shown that the parent compound, $KNbO_3$ (KNO), can be doped with Ba and Ni at various controlled stoichiometries in order to produce $[KNbO_3]_{1-x}[BaNi_{0.5}Nb_{0.5}O_{3-\delta}]_x$. This perovskite oxide material has been shown to exhibit both ferroelectricity and a wide variation of the direct bandgap in the range 1.1–3.8 electronvolts.[8] In the case of x = 0.1, KBNNO is polar at room temperature, has a direct bandgap of 1.39 eV[8] and a recorded photocurrent density much larger than that of classic ceramic ferroelectrics, for example $50\times$ larger than $(Pb,La)(Zr,Ti)O_3$. A common problem in most ferroelectric photovoltaic materials is the wide band gap (usually >3.0 eV), which makes absorbing visible light a challenge. Introducing the Ni^{2+} onto the B-site and oxygen vacancies by mixing $BaNi_{0.5}Nb_{0.5}O_{3-\delta}$ (BNNO) with $KNbO_3$ effectively allows for a tunable band gap of 1.1–2.0 eV,[8,9] which is much lower than the band gap of $KNbO_3$, 3.16 eV.[10] The ability of KBNNO to absorb three to six times more solar energy than the current ferroelectric materials suggests a route to viable ferroelectric semiconductor-based cells for solar energy conversion and motivates the exploration of synthetic routes to KBNNO and its analogues. In this paper we demonstrate that sol–gel derived chemical solution processing methods can be readily adapted for the synthesis of $KNbO_3$, and show that doping to produce KBNNO, with compositions x = 0.1–0.3, is achievable. We performed structural and morphological characterization of these ferroelectric nanocrystalline systems, combined with in depth analysis of their dielectric properties in nano-structured and nanocomposite form.

Given that KBNNO can be viewed as a doped version of KNO, the first obvious route to making the compound is by ceramic processing at high temperatures, but such methods limit the imagination in terms of how this material may ultimately be adopted in device technology. A universal challenge, both in the commercial and university R&D settings is to develop alternatives to high temperature ceramic processing (firing, sintering or calcination), that can allow for a broader range of ceramic technologies to be integrated more effectively with circuit design, and open more technology avenues such as flexible electronics, novel device topologies, and roll-to-roll fabrication.[11–13] In this work we put forward a chemical solution method to synthesize both $KNbO_3$ and KBNNO by a hybrid sol–gel, non-aqueous synthesis known as gel collection.[14,15] It is a precursor driven technique that allows for doping of nanocrystalline $KNbO_3$ with Ba and Ni to make $[KNbO_3]_{1-x}[BaNi_{0.5}Nb_{0.5}O_{3-\delta}]_x$ (KBNNO). We previously reported a simple, green and scalable "self-collection" growth method to produce uniform and aggregate-free colloidal perovskite oxide nanocrystals including $BaTiO_3$ (BT), $Ba_xSr_{1-x}TiO_3$ (BST) and $BaSrTiHfO_3$ (BSTH) in high crystallinity and high purity.[16] The synthesis approach is solution processed, based on the sol–gel transformation of metal alkoxides in alcohol solvents with controlled or stoichiometric amounts of water and in the stark absence of surfactants and stabilizers. Under a static condition, the nanoscale hydrolysis of the metal alkoxides accomplishes a complete transformation to fully crystallized single domain perovskite nanocrystals with a passivated surface layer of hydroxyl/alkyl groups, such that the as-synthesized

nanocrystals can exist in the form of super-stable and transparent sol, or self-accumulate to form a highly crystalline solid gel monolith of nearly 100% yield for easy separation/purification. We sought to adapt this method for the synthesis of KNO and KBNNO, and then study the structure and dielectric properties that can be attained.

Experimental

Potassium ethoxide (KOC_2H_5) 24 wt% in ethanol and niobium ethoxide ($Nb(OC_2H_5)_5$) 99.95% trace metals basis were purchased from Sigma-Aldrich®. Nickel 2-methoxyethoxide ($Ni(O(CH_2)_2OCH_3)_2$) 5% w/v in 2-methoxyethanol and barium ethoxide ($Ba(OC_2H_5)_2$) 99.5% (metals basis), 10% w/v in ethanol were purchased from Alfa Aesar®. Pure ethanol (200 proof) was purchased from Decon Labs, Inc. All chemicals were used without further purification. In a typical synthesis, mmol amounts of alkoxide precursors were used according to the target stoichiometry. For example, for the synthesis of $KNbO_3$, 1.6 mmol of KOC_2H_5 was combined with 1.6 mmol of $Nb(OC_2H_5)_5$, and for the synthesis of $[KNbO_3]_{0.9}[BaNi_{0.5}Nb_{0.5}O_{3-\delta}]_{0.1}$, 1.44 (1.6 × 0.9) mmol of KOC_2H_5 was combined with 1.52 ((1.6 × 0.9) + (0.5 × 1.6 × 0.1)) mmol of $Nb(OC_2H_5)_5$, 0.16 (1.6 × 0.1) mmol of $Ba(OC_2H_5)_2$ and 0.08 mmol of $Ni(O(CH_2)_2OCH_3)_2$.

All compounds were synthesized under nitrogen in a glovebox by adding stoichiometric amounts of KOC_2H_5 and $Nb(OC_2H_5)_5$ to 40 mL of ethanol and magnetically stirring for 30 min. 2 mL of deionized water was then added drop-wise via a 5 mL syringe. A white precipitate formed and the resulting suspension was stirred for another 10 min. The suspension was then transferred out of the glovebox and into a Teflon-lined stainless steel autoclave. The autoclave was then heated to 180 °C for 48 h. The white gel produced from this process is collected by centrifugation (8500 rpm for 20 minutes), and then heated to 525 °C in air. A white powder is produced. The calcination temperature of 525 °C was found to be the minimum optimal temperature for producing crystalline material. KBNNO was synthesized using $Ba(OC_2H_5)_2$ and $Ni(O(CH_2)_2OCH_3)_2$ in addition to KOC_2H_5 and $Nb(OC_2H_5)_5$. The powders were collected and used as is for characterization.

Characterization

The resulting nanopowders were characterized by X-ray powder diffraction (XRD), Raman spectroscopy, transmission electron microscopy (TEM), and scanning electron microscopy (SEM). The XRD measurements were performed on a PANalytical X'Pert Pro using Cu Kα radiation. The Raman spectra were measured on a home-built microscopic Raman spectrometer with a 40× objective and a Princeton Instruments Raman detector (model #PK244M-01AA-C3) using an 1800 g mm^{-1} grating with an air-cooled CCD detector. All Raman spectra were taken with a 488 nm excitation wavelength. In order to resolve the active modes, Origin (OriginLab, Northampton, MA) software was used. Samples for the TEM were prepared by placing 5 μl of the nanocrystalline powder dispersed in ethanol solution on a carbon coated copper grid. TEM micrographs and energy-dispersive X-ray spectroscopy

(EDS) were recorded on a JEOL 2100 microscope. Cross sectional SEM samples of the 0–3 nanocomposite were prepared by freeze cracking the nanocomposite pellets with liquid nitrogen. The SEM micrographs were recorded on a Supra 55 SEM.

Impedance analysis was performed on all samples in order to measure the frequency dependent dielectric constant. The powders were pressed into a pellet by applying 15–20 MPa of pressure using a Cyky 12T Laboratory manual powder metallurgy press machine and a 0–3 nanocomposite was made by applying an appropriate amount (enough to cover the surface) of furfuryl alcohol (FA) to the surface of the pellet. The nanocomposite was then heated to 100 °C for 6 hours to encourage polymerization into poly furfuryl alcohol (PFA). A piece of copper conductive adhesive tape was placed on a glass substrate and then a silver contact bottom electrode was made using MG Chemicals 2 part silver conductive epoxy. The 0–3 nanocomposite pellet was then placed on top of this electrode and a top circular electrode was made on top of the pellet. The capacitance and dielectric loss tangent were measured over the range of 100 Hz–2 MHz using an Agilent E4980A Precision LCR Meter.

Results and discussion

Structural characterization

Gel collection was applied to the synthesis of $KNbO_3$ and KBNNO ceramics in which nanocrystalline powders can be produced from solvothermal treatment of alkoxide precursors, following a low temperature (<550 °C) calcination step. In order to generate KBNNO, $[KNbO_3]_{1-x}[BaNi_{0.5}Nb_{0.5}O_{3-\delta}]_x$, it is a reasonable thought experiment to start with KNO ($KNbO_3$) and introduce increasing amounts of Ba and Ni dopants to the lattice. The XRD patterns of $KNbO_3$ and KBNNO ceramics for $x = 0.1$, 0.2 and 0.3 are shown in Fig. 1. The Bragg reflections of $KNbO_3$ ($x = 0$) can be indexed to the orthorhombic crystal system of $Amm2$,[17] typically observed for this structure. In order to confirm the structure, nanopowders of $KNbO_3$ were further heated to 700 °C and 900 °C (ESI,† Fig. S2), showing an increase in the resolution and intensities of the XRD profile. It was also possible to perform Rietveld analysis on these powder spectra, including the data acquired at 525 °C. The unit cell parameters obtained for $KNbO_3$ are $a = 3.99323$ Å, $b = 5.68794$ Å, and $c = 5.70066$ Å. Rietveld simulation confirmed the structure to be the orthorhombic crystal system with space group $Amm2$, details are provided in the ESI† (Fig. S1, and Table S1).

In the case of KBNNO for $x = 0.1–0.3$ one can observe a change in the powder diffraction profile, in which the Bragg reflections index well to the cubic crystal system of $Pm3m$.[18] In particular the distinction between the (110)/(001) and (220)/(002) Bragg reflections in peak sets at around 22 and 45 2θ, clearly observable in the case of $KNbO_3$, converge and indexing to (001) and (002) becomes preferable. This appears to be an indication of the onset of a transformation of the crystal structure from orthorhombic to cubic, with increasing value of x. This is also consistent with previously reported XRD data of KBNNO prepared by traditional solid state synthesis.[8] Due to nanocrystallite
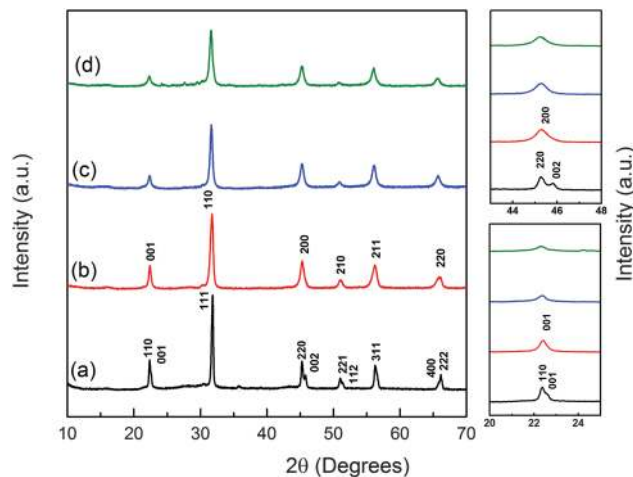

Fig. 1 XRD patterns of: (a) $KNbO_3$, (b–d) $[KNbO_3]_{1-x}[BaNi_{0.5}Nb_{0.5}O_{3-\delta}]_x$ KBNNO (b) $x = 0.1$, (c) $x = 0.2$, (d) $x = 0.3$, all samples shown were sintered to 525 °C for 2 h.

size Bragg reflection broadening, it is difficult to determine a shift in 2θ due to doping of Ba^{2+} and Ni^{2+} into the crystal lattice. The larger Ba^{2+} ionic radius in comparison to K^+ should induce a change in the lattice parameters but Rietveld analysis of this high symmetry set of Bragg reflections was inconclusive, due to the number of possible space groups, and variable coordinates for Ba and Ni. DFT calculations on KBNNO have previously relied on a structural model using a 60 atom perovskite-based supercell.[8] The introduction of a BNNO portion into the crystal lattice of $KNbO_3$ appears to change the morphology of the crystal to cubic with increasing BNNO as seen in Fig. 2. By KBNNO $x = 0.3$, the nanocrystalline powders are completely cubic.

The samples were further evaluated for morphology and degree of crystallinity by transmission electron microscopy (Fig. 2). All samples were observed to be nanocrystalline powders. The morphology of KNO appeared to adopt a more rounded character whereas the KBNNO samples ($x = 0.1$ to 0.3) had well defined cubic edges. The average particle size may have been affected by the addition of BNNO into the crystal lattice. $KNbO_3$ had an average particle size of ~ 20 nm whereas with increasing BNNO concentration, we were able to attain crystals of 20 nm and smaller. All samples are polycrystalline as shown by the selected area diffraction in Fig. 2.

To distinguish between KNO and KBNNO, and to further confirm inclusion of the Ba and Ni ions into the lattice, Raman spectroscopy was performed on all samples. The recorded Raman spectra are shown in Fig. 3. There are 4 modes in the low to mid wavenumber region (100–400 cm^{-1}). The $A_1(TO,LO)$ mode at ~ 280 cm^{-1} corresponds to a BO_6 bending vibration,[9] while the $A_1(TO)$ and the $B_1(TO)$ at ~ 245 cm^{-1} and 188 cm^{-1} respectively, are indicative of a long-range polar order as seen by Luisman et al.[19] The $B_2(TO)$ mode has been reported by Quittet et al.[20] and Shen et al.[21] A weak overtone is seen at ~ 890 cm^{-1} in the $KNbO_3$ Raman spectrum and is a combination of the $B_2(TO)$, $A_1(TO)$ (245 cm^{-1}) and the $B_1(TO)$ (535 cm^{-1}). Upon increasing x value ($x \geq 0.1$) the Raman spectrum changes rather
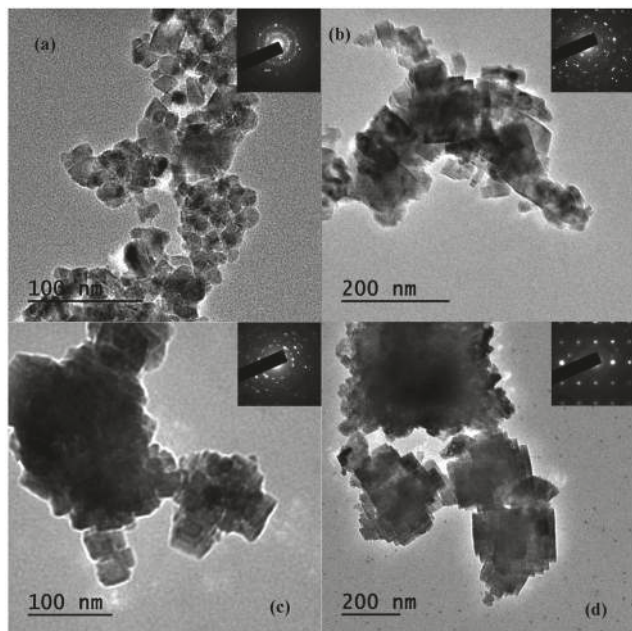
Fig. 2 TEM images of (a) $KNbO_3$, (b–d) $[KNbO_3]_{1−x}[BaNi_{0.5}Nb_{0.5}O_{3−\delta}]_x$ KBNNO (b) $x = 0.1$, (c) $x = 0.2$, (d) $x = 0.3$, all samples shown were sintered to 525 °C for 2 h. Insets: Corresponding selected area electron diffraction patterns.

dramatically as seen in Fig. 3(b). Most notable is the disappearance of the A_1(TO,LO) mode at ~ 296 $cm^{−1}$ in favor of a broadening of the A_1(TO) mode as denoted by ν_3. It is important to note that there is a shift in frequency in the A_1(TO) mode at ~ 605 $cm^{−1}$ and B_1(TO) mode at ~ 534 $cm^{−1}$ as denoted by ν_4 and ν_5 which are at ~ 537 $cm^{−1}$ and ~ 581 $cm^{−1}$ respectively. Furthermore, these two modes, ν_4 and ν_5, coalesce to form one broad mode at ~ 563 $cm^{−1}$ as $x > 0$, which can be attributed to the change in crystal structure from orthorhombic ($KNbO_3$) to cubic (KBNNO $x \geq 0.1$). The A_1(LO) mode (~ 834 $cm^{−1}$) shows a shift to ~ 824 $cm^{−1}$ and a new mode, denoted by ν_7 arises with increasing Ni^{2+} concentration at ~ 880 $cm^{−1}$, which is in agreement with Zhou et al.,[9] and corresponds to a BO_6 octahedral stretching due to the presence of Ni^{2+}. There is also a frequency

dip at 200 $cm^{−1}$ in Fig. 3(a) and (b) along with the above mentioned peaks A_1(LO) and the ν_6 peak which are observed by Grinberg et al.[8] and Zhou et al.[9] which have been identified as signatures of ferroelectricity in $KNbO_3$-based solid solutions.[22]

Synthesis mechanism

Solution processed methods for preparing high quality inorganic oxide films and composites, especially ones that can be generalized[23] are of great interest.[24,25] Low temperature chemical methods may prove cheap and easy to integrate within an existing manufacturing framework, or prove compatible with a disruptive approach, such as printing or spray coating. Second, R&D efforts can take advantage of low temperature techniques to discover new compounds due to the ability of introducing dopants *via* chemical reaction.[26–29] In traditional sol–gel reactions, transformation to an extended amorphous inorganic polymer network proceeds through acid/base catalyzed hydrolysis in water, of metal alkoxides and metal chlorides, and the sol–gel is continuous, within liquid and gel.[30] The reactions take place in air with little or no attention paid to the effect of O_2, CO_2 and mineral contaminants, be they dissolved in the solvents or at the interface, however, both oxygen and dissolved carbonic species can greatly influence the reaction pathway. Oxygen and water both oxidize the metal centers but *via* different intermediates, and the formation of carbonates is highly thermodynamically favored, and can hamper opportunity for more mixed metal/valence structures. In the process we outline here, the initialization of the reaction takes place at near room temperatures. Non-aqueous polar protic solvent environments are used without ligands to avoid (i) an abundance of organic content, and (ii) interference with the kinetics of oxide formation. Metal-oxide bond formation is initiated by stoichiometric quantities of water – H_2O is used as molar reactant – but the gel is not miscible with the solvent and precipitates out. Unlike sol–gel, the controlled use of hydrolysis agents is simultaneously performed with rigorous exclusion of O_2, CO_2 *etc.* Rather than controlling nucleation and growth using passivating ligands (as is the case in nanoparticle synthesis), the consumption of reactant in the alcohol medium at near room temperature prevents
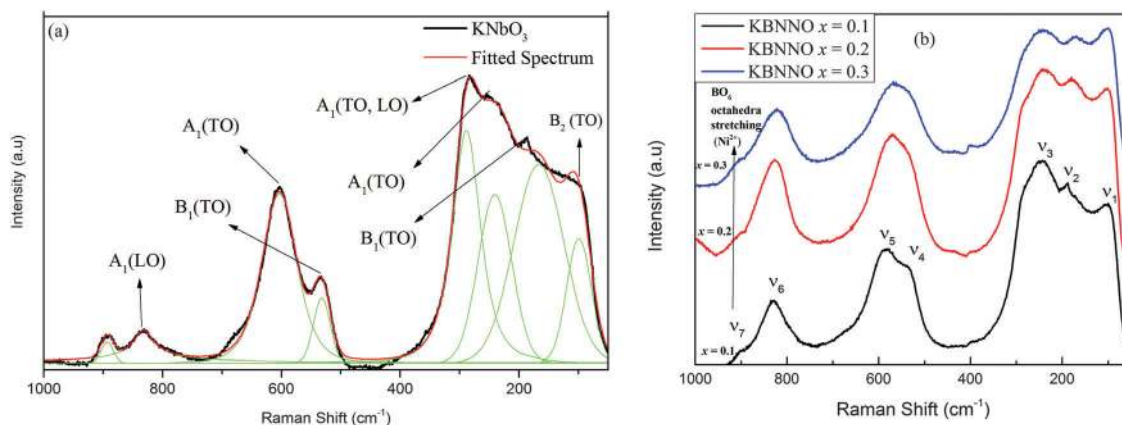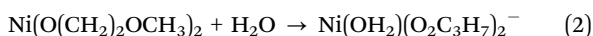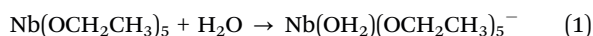

Fig. 3 (a) Raman spectrum of $KNbO_3$ measured with an excitation wavelength of 488 nm (black line), fitted spectrum (red line) resolved modes (green line), (b) Raman spectra of KBNNO $x = 0.1$–0.3 with an excitation wavelength of 488 nm.

further growth. The surface states of oxide perovskite nano-crystals produced by this method have been shown to be short chain groups (methoxy, ethoxy) in low density.[15]

$KNbO_3$ is a well-known perovskite oxide with the general structure of ABO_3 where Nb resides in the octahedron surrounded by the 6 O atoms. Upon addition of nickel ions into the unit cell, oxygen vacancies are generated[8] with local structure $Ni^{2+}-V_O-Ni^{2+}$ and $Ni^{2+}-V_O-Nb^{5+}$ due to charge balancing. We further investigated the chemical route for synthesizing $KNbO_3$ and KBNNO (mechanism provided in ESI,† Fig. S3), for which the molecular precursors are metal alkoxides. Our postulated synthesis mechanism is summarized as follows: on addition of a stoichiometric amount of water to the solution of KOC_2H_5 and $Nb(OC_2H_5)_5$ in ethanol for $KNbO_3$, and KOC_2H_5, $Ba(OC_2H_5)_2$, $Nb(OC_2H_5)_5$, and $Ni(O_2C_3H_7)_2$ in ethanol, nucleophilic attack by the H_2O molecule on the positively charged Nb and Ni atoms leads to an intermediate octahedrally coordinated Nb and a tri-coordinated Ni atom center:

$$Nb(OCH_2CH_3)_5 + H_2O \rightarrow Nb(OH_2)(OCH_2CH_3)_5{}^- \quad (1)$$

$$Ni(O(CH_2)_2OCH_3)_2 + H_2O \rightarrow Ni(OH_2)(O_2C_3H_7)_2{}^- \quad (2)$$

$Nb(OCH_2CH_3)_5$ is likely the driving force of reactivity in this reaction as it is the most electrophilic of the molecular precursors similar to $Ti(OiPr)_4$ in the synthesis of BST nanoparticles.[15] The close proximity of $Ni(O(CH_2)_2OCH_3)_2$ due to the homogenous mixing in solution allows for even substitution into the octahedron which may otherwise not occur. The counterions, Ba^{2+} and K^+ then coordinate with the negative six-coordinated $Nb(OH_2)(OCH_2CH_3)_5{}^-$ and $Ni(OH_2)(O_2C_3H_7)_2{}^-$ in order to provide charge balancing. There is then a transfer of a proton from the H_2O molecule to the negatively charged alkoxy group, ethoxide for Nb, and 2-methoxyethoxide for Ni. The transfer of the proton leads to the elimination (alkoxolation) of the corresponding alcohols, $HOCH_2CH_3$ and $HO(CH_2)_2CH_3$. At this point the solution is put into a stainless steel Teflon lined autoclave at 180 °C for 2 days. This aids the process of the formation of the Nb–O–Nb and Nb–O–Ni bonds through polymerization. The amorphous powders are then collected by centrifugation and the condensation/crystallization process occurs upon sintering at <525 °C. Previous syntheses of KBNNO involved the use of stoichiometric quantities of dried K_2CO_3, $BaCO_3$, NiO, and N_2O_5 powders. The powders were ball-milled and then calcined at 900 °C and then further sintered to 1050–1250 °C.[8,9] The chemical route to the synthesis of KBNNO described here provides a lower temperature of crystallization due (i) the hydrolysis of metal alkoxides and (ii) the final crystallite size obtained.

Dielectric properties

The dielectric properties of nanocrystalline KNO and KBNNO were investigated in both compressed pellet form and as a polymer–nanoparticle 0–3 nanocomposite. The permittivity values were analyzed in the context of a full assessment of error and uncertainties, and compared with literature reported values for the bulk. Given that both materials are ferroelectric,

high values of permittivity are expected, however, interpretation of the frequency dependent measurement requires care, due to the nature of how the dielectric constant is obtained for such a materials sample, which could be described as inhomogeneous. In such cases one must account for the interstitial void space and electrode–dielectric interface that can contribute to charge effects. The Maxwell–Wagner–Sillars polarization effect is essentially the observation of charge phenomena (space charge, adsorbed mobile species) when acquiring dielectric measurements. The effect occurs either at inner dielectric boundary layers on a mesoscopic scale, or at the external electrode–sample interface on a macroscopic scale. In both cases separation of charge can occur, which contributes to the low frequency dielectric behavior and to increased dielectric loss.

In the samples prepared here, an effective medium approximation is being applied *de facto*, when the impedance measurement is acquired, to a 0–3 nanocomposite. In the first case, the 0–3 host–filler construction is air–nanoparticle (Fig. 4), and in the second case the 0–3 host–filler construction is polymer–nanoparticle (Fig. 5). An important question that arises is how much of the contribution to the effective dielectric constant is due to the intrinsic behavior of the nanocrystalline KNO/KBNNO materials (originating from ion displacement from within the lattice), *versus* the contribution of mobile charges on the surface of, or between the nanoparticles.

Nanocrystalline KNO and KBNNO were first pressed into a pellet (15–20 MPa) with dimensions of approximately 5 mm diameter and 100 μm thickness. The nanostructure of the pressed pellet was taken by SEM (Fig. 6) and shows the uniform particles contiguously packed. These pellets were subsequently prepared for impedance analysis. The measurement of this 0–3 air–nanoparticle pellet was acquired, mainly for comparison, and to observe the contribution of Maxwell–Wagner–Sillar polarization. In order to measure the dielectric properties without the interference of space charge and surface species from the pure nanocrystalline sample, nanoparticle–polymer composites were prepared. Void space between the nanoparticles can be eliminated with the introduction of a polymer, backfilled as a monomer and polymerized *in situ*. We previously reported the use of poly furfuryl alcohol as an ideal polymer of known dielectric constant for this purpose.[16] Furfuryl alcohol (2-furanmethanol, referred to by some vendors as furfural alcohol, abbreviated here as FA) is a versatile solvent that shows good affinity to the surface of oxides of this kind and good compatibility with various solvents. The polymerization process occurs with heating in the presence of the nanoparticle surface without the addition of any acid catalyst. FA was therefore used as an effective void filler as well as a polymerizable solvent to prepare densely packed nanocrystal/polymer 0–3 composites with dramatically improved and stabilized dielectric properties over a wide range of frequencies and improved mechanical strength and adhesion. The 0–3 nanocomposite was made by applying enough furfuryl alcohol (FA) to cover the surface of the pellet. The nanocomposite was then heated to 100 °C for 6 hours to encourage polymerization into poly furfuryl alcohol (PFA). The mechanism of FA acid-catalyzed polymerization of furfuryl alcohol
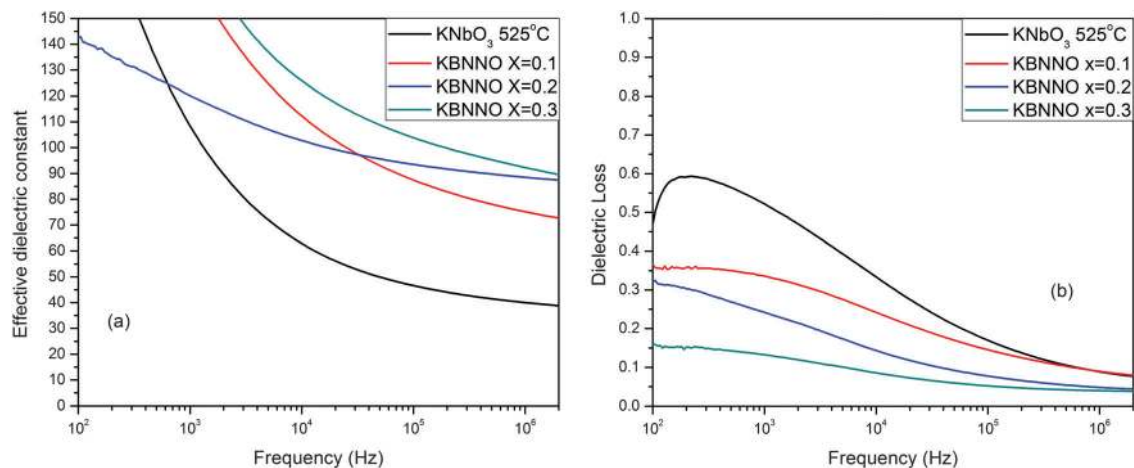
Fig. 4 (a) Effective dielectric constant of $KNbO_3$ and KBNNO x = 0.1–0.3 nanoparticle pellets over a frequency range of 100 Hz–2 MHz, (b) dielectric loss of $KNbO_3$ and KBNNO x = 0.1–0.3 nanocomposite pellets over a frequency range of 100 Hz–2 MHz. The pellets are essentially a nanoparticle/air 0–3 nanocomposite. The volume fraction of nanoparticle is presented in Table 1.
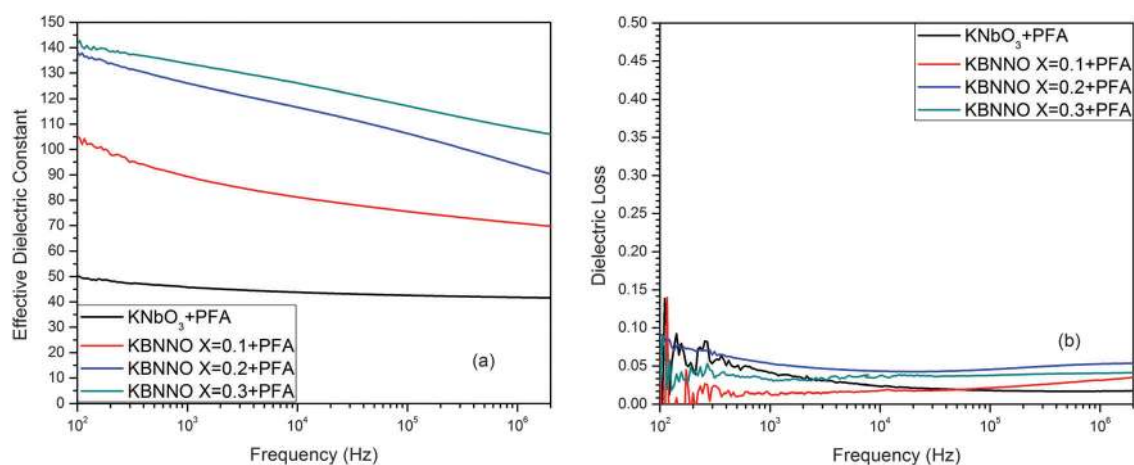

Fig. 5 (a) Effective dielectric constant of $KNbO_3$/PFA and KBNNO/PFA x = 0.1–0.3 nanocomposites over the frequency range of 100 kHz–2 MHz, (b) dielectric loss of $KNbO_3$/PFA and KBNNO/PFA x = 0.1–0.3 nanocomposites over the frequency range of 100 kHz–2 MHz.

(the acid-catalyzed chain extension of –CH_2OH ended furfuryl alcohol oligomers) has been described previously by Dunlop and Peters, and subsequent reports.[31,32] It is assumed that the –CH_2OH groups react with the C5 carbon of a neighboring furfuryl alcohol moiety to produce a polymer with methylene cross links (see ESI,† Fig. S9), combined with the mutual reaction of –CH_2OH groups to produce methylene ether links in both cases with the elimination of water. The methylene ether group undergoes decomposition, especially at elevated temperature (>90 °C) with the elimination of formaldehyde (CH_2O) to produce methylene cross-links. During nanocomposite formation, the elimination of H_2O and CH_2O are observed, and it is supposed that the nanoparticle surface alkoxy groups (–ROH) combined with heating provide sufficient conditions for FA polymerization.

The dielectric constant of the $KNbO_3$/PFA and KBNNO x = 0.1–0.3/PFA nanocomposites was measured over the frequency range of 100 Hz to 2 MHz. The dielectric loss of these nanocomposites was also measured on the same instrument. It is shown, in the cross sectional analysis in Fig. 6, that the PFA polymer infiltrated the pellet and filled the void space very well. The confirmation by SEM, combined with the notable improvement in the dielectric measurement, namely the observation of a straighter line as a function of frequency, provides strong evidence that (i) the composite pellet is a 0–3 construction, composed of PFA/KN-material and not void space; (ii) the effective permittivity acquired using impedance analysis is overwhelmingly due to the intrinsic nature of the material, and not from Maxwell–Wagner–Sillars (M–W–S) polarization effects. The second issue of whether charge accumulation is occurring between the material and the electrode is also important to analyze. The dielectric loss values are observed to be in the range 0.02–0.05, suggesting that the contacts are of sufficient quality to proceed with analysis of the intrinsic dielectric constant. These dielectric loss values are, we believe, very promising, for bench top measurements of capacitance under normal atmospheres.
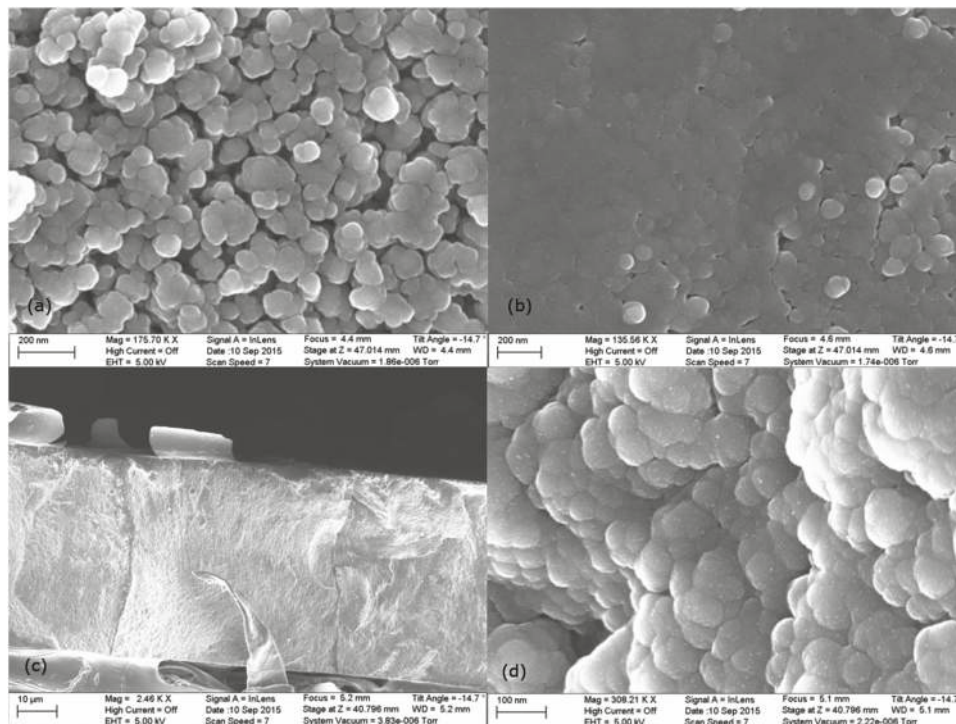
Fig. 6 (a) SEM top view of pellet of KBNNO ($x = 0.2$) without PFA showing a relatively uniform nanostructured morphology with an average particle of size of ~ 20 nm, (b) SEM top view of pellet of KBNNO ($x = 0.2$) with PFA infiltration, (c) SEM cross section of pellet of KBNNO ($x = 0.2$) with PFA infiltration, (d) SEM cross section of pellet of KBNNO ($x = 0.2$) with PFA infiltration.

The nanocomposite pellets can be considered a 0–3 type composite made up of nanocrystal fillers (granular) with high k, distributed evenly in a continuous dielectric PFA polymer host matrix. It is important to assess the effective dielectric constant, ε_{eff}, of the 0–3 nanocomposite as a whole by taking into account the volume fraction of the high k dielectric nanocrystal. If the volume fraction of the high k component is not in the majority, there will be a negligible impact on ε_{eff}.[21] A modified approach to the Kerner model[33,34] with correction of the volume fraction can be used in order to calculate the effective dielectric constant and is expressed as:

$$\varepsilon_{\text{eff}} = \frac{\varepsilon_{\text{h}} \times v_{\text{h}} + \varepsilon_{\text{f}} \times v_{\text{f}} \times (A)(B)}{v_{\text{h}} + v_{\text{f}} \times (A)(B)},$$

$$\text{where } A = \frac{3\varepsilon_{\text{h}}}{\varepsilon_{\text{f}} + 2\varepsilon_{\text{h}}} \text{ and } B = 1 + \frac{3v_{\text{f}} \times (\varepsilon_{\text{f}} - \varepsilon_{\text{h}})}{\varepsilon_{\text{f}} + 2\varepsilon_{\text{h}}}$$

where ε_{h} and ε_{f} are the dielectric constants of the host and the filler respectively and v_{h} and v_{f} are the volume fractions of the host and filler respectively. The Kerner model[34] along with its variants[33,35] take into account the influence of particle–particle dipolar interactions as well as their effects on the dielectric medium in which they are dispersed in. As a micromechanical model, the Kerner model attempts to achieve a reasonable approximation for calculating the dielectric constants based on a high volume fraction of filler spherical particles.

A pellet of pure nanocrystal, as seen in Fig. 6(a) is porous and has significant void space due to the packing of the nanocrystals. It will also absorb molecules from the air over time (H_2O/O_2),

which will contribute to a large spike in the dielectric constant along with interfacial polarizations (space charge) as seen in Fig. 4(a). This higher dielectric constant and dielectric loss is observed in the lower frequency range (~ 100 Hz) and is due to the aforementioned space charges and surface absorbed molecules whose polarization direction cannot deal with the switching frequency of the AC electric field.[21] The dielectric loss and dielectric constant eventually smooth out at higher frequency ($< 10^4$ Hz) because the intrinsic dielectric properties of the $KNbO_3$ or KBNNO nanocrystal become dominant.

In striking contrast, the $KNbO_3$/PFA and KBNNO/PFA nanocomposites show very stable dielectric loss and dielectric constant over a wide range of frequencies (Fig. 5). As expected, the ε_{eff} decreases moderately towards higher frequencies and the dielectric loss shows a slight increase. The overall stability in ε_{eff} and loss is due to the infiltration of the PFA polymer, filling of the majority of the void space between the nanocrystals (Fig. 6(a) before, Fig. 6(b) after infiltration). Although air molecules may still be present within the polymer portion, the filling of the void space significantly suppresses space charge accumulation and M–W–S effects at the material–electrode interface.

The effective dielectric constant of the nanocomposites were calculated based on the generalized technique of impedance analysis and conversion to capacitance, in this case using an Agilent E4980A Precision LCR Meter. The measurement requires a precise value of area (A) of the electrodes and thickness (d) of the nanocomposite, in order to determine the effective dielectric constant, ε_{eff}, from $C = (\varepsilon_{\text{eff}}\varepsilon_0)\frac{A}{d}$. Values are presented in Table 1.

Table 1 Comparison of dielectric properties of $KNbO_3$/PFA and KBNNO/PFA nanocomposites (taken at 1 MHz)

Sample	Effective dielectric constant, ε_{eff}, of nanocomposite	Dielectric loss	Volume fraction of nanocrystals (%)
$KNbO_3$/PFA nanocomposite	41.2	0.02	~51
KBNNO $x = 0.1$/PFA nanocomposite	70.8	0.03	~67
KBNNO $x = 0.2$/PFA nanocomposite	94.0	0.05	~67
KBNNO $x = 0.3$/PFA nanocomposite	108.3	0.04	~68

A full description of how the measurement is calculated, combined with a comprehensive error analysis, is provided in the ESI† (S10). The ε_{eff} of the nanocomposites was observed to increase with increasing x. This is consistent with the high frequency ε_{eff} values for the nanoparticle pellets without polymer (Fig. 4): at high frequency a value closer to the intrinsic value of the material can be assumed.

The determination of the average dielectric constant of individual nanoparticles of the oxide embedded in a host matrix (the PFA filler) was performed using the Kerner model described above. The Kerner model is a treatment for a high volume fraction of filler and a lower volume fraction of host, based on spherical particles. We therefore observe that our calculations of dielectric constants will depend on (i) accuracy of the volume fraction calculations, based on volume and mass of the pellet; (ii) accuracy of the Kerner model, including principles and practice. The volume fraction calculation and uncertainties can be determined based on volume, mass and density of filler (see ESI,† S10). It was found that the Kerner model cannot account for a high effective dielectric constant at these calculated volume fractions. Given the calculated error in the effective dielectric, it is very difficult to obtain a reasonable value for the intrinsic dielectric constant of the nanoparticle using the Kerner model.

Another composite model has been proposed by M. Ezzat et al.,[37] which takes into account particle shape/orientation as well as the interphase spacing between nanoparticles. The model is based on the interphase power-law model[37] yet with an introduced technique to predict the interphase dielectric constant. Within the interphase may lie air, matrix, and filler atoms, all of which may affect the interactions between nanoparticles embedded in a nanocomposite. When modeling a nanocomposite consisting of nanoparticle fillers and a polymer host, there is a considerable amount of air in the interphase region. Therefore the interphase dielectric constant can be attributed to polymer and air:

$$\varepsilon_3^\beta = \varepsilon_2^\beta + \varphi_a(1 - \varepsilon_2^\beta)$$

Above, ε_3 is the dielectric constant of the interphase, ε_2 is the dielectric constant of the polymer, φ_a is the volume fraction of air within the interphase, and β is a dimensionless parameter depending on the shape and orientation of the filler. For spherical nanoparticles, $\beta = 1/3$. An overall formula for the

effective dielectric constant (ε_{eff}) using the interphase dielectric can written as:

$$\varepsilon_{eff}^\beta = \varphi_1\varepsilon_1^\beta + (1 - \varphi_1)\varepsilon_2^\beta + \varphi'(1 - \varepsilon_2^\beta)$$

Where φ_1 is the filler volume fraction, ε_1 is the filler dielectric constant, and φ' is:

$$\varphi' = \varphi_1\frac{1 - \varphi_1}{1 + \varphi_1}$$

At volume fractions lower than ~0.80, the interactions of nanoparticles with the surrounding interphase becomes important to incorporate into a standard field approximation. The dielectric constant of KNO and KBNNO $x = 0.1$–0.3 was determined by using the modified interphase model[36] and was calculated to be 154, 180, 225, and 255 respectively. In comparison, a range of values have been reported previously with varying experimental parameters, such as frequency and morphology: Krad et al.[38] synthesized nanoplates of $KNbO_3$ and obtained a value of ~200 at 1 MHz at 100 °C, Birol et al.[39] report a value of ≥1000 at 1 MHz at room temperature for the solid state synthesis of $KNbO_3$, and Shirane et al.[40] reported a value of ≥500 at 10 kHz at room temperature for the single crystalline orthorhombic $KNbO_3$. Additional values are reported.[41–44] KBNNO, being a relatively new material, did not have as many tabulated values to compare to except for Grinberg et al.[8] in which the dielectric constant, k, for bulk KBNNO is ~520 for $x = 0.1$, ~310 for $x = 0.2$, and ~280 for $x = 0.3$ in the temperature range 300–600 °C. There is an apparent absence of phase dependent behavior in this range until ≥600 °C, at which point a decrease in k for higher x and an increase in k for lower x is observed. The frequency of the measurement was not provided, making a direct comparison difficult, but it would appear that the opposite trend was observed in the case of nanocrystalline versions of KBNNO at 1 MHz, taking into account error margins in the assessed values. It could be that the bulk KBNNO has ferroelectric domains that are contributing to the dielectric values observed (which subsequently reverse at high T commensurate with a phase transition), and that in the case of the 20 nm nanocrystalline composite measured here, a suppression of this effect is observed and the contribution of the Ba, Ni doping, gives an increase in the k, with increasing dopant concentration. Furthermore, the orientation dependence of the crystallites, known to greatly affect the electrical response,[45,46] may be playing a role in the outcome. In the case of PFA–KBNNO nanocomposites, the crystallites are not perfectly spherical and are randomly oriented throughout the matrix, significantly different than a bulk crystal. We additionally suggest that the effect of crystallite size has a strong influence on the ferroelectric behavior of the material, reflected in the dielectric measurement, and consistent with observations in other perovskite systems:[47] a lower value in dielectric constant is to be expected for nanocrystalline KNO and KBNNO $x = 0.1$–0.3 synthesized by gel collection because of the size of the nanoparticles (~20 nm). It is proposed that a size dependent suppression of ferroelectricity in the nanoparticles could likely lead to a lowering of the dielectric constant. This supposed size dependent suppression is also observable in the

Raman spectrum, noticeable in the less pronounced, but still present frequency dip in the Raman spectrum at 200 cm^{-1}, as shown in Fig. 3(a) and (b).

Conclusion

In conclusion, nanocrystalline samples of $KNbO_3$ and KBNNO x = 0.1–0.3 were synthesized through use of the gel collection method, shown to be well crystallized and on the order of 15–20 nm depending on concentration of BNNO. Structural characterization shows an orthorhombic to cubic phase transition upon BNNO substitution into the crystal unit cell. A method for preparing dense PFA–perovskite oxide composites produced 0–3 nanocomposites with effective dielectric constants of 41.2 for $KNbO_3$, 70.8 for KBNNO x = 0.1, 94.0 for KBNNO x = 0.2, and 108.3 for KBNNO x = 0.3. A full error analysis was conducted in order to ascertain the accuracy of the dielectric measurements. In the case of the PFA–KBO/KBNNO nanocomposites, we report a stable dielectric constant and low dielectric loss over the frequency range 100 Hz–2 MHz. Through the use of the modified interphase model,[40] the dielectric constants of $KNbO_3$ and KBNNO x = 0.1–0.3 were calculated to be 154, 180, 225, and 255 respectively. These values are high when compared to many other oxide materials and demonstrate the potential for high energy density capacitance. Given the size of the nanoparticles, a size dependent suppression of ferroelectricity, further supported through Raman spectroscopy, is proposed to be the cause of a decrease in the dielectric constants when compared to bulk KNO and KBNNO.

Acknowledgements

References

1   J. Rödel, W. Jo, K. T. P. Serfert, E. Anton and T. Granzow, *J. Am. Ceram. Soc.*, 2009, **92**, 1153–1177.
2   Y. Saito, H. Takao, T. Tani, T. Nonoyama, K. Takatori, T. Homma, T. Nagaya and M. Nakamura, *Nature*, 2004, **432**, 84–87.
3   D. Xue and S. Zhang, *Chem. Phys. Lett.*, 1998, **291**, 401–406.
4   E. S. Polzik and H. J. Kimble, *Opt. Lett.*, 1991, **16**, 1400–1402.
5   J. W. Bennett, I. Grinberg and A. M. Rappe, *J. Am. Chem. Soc.*, 2008, **130**, 17409–17412.
6   G. Y. Gou, J. W. Bennett, H. Takenaka and A. M. Rappe, *Phys. Rev. B: Condens. Matter Mater. Phys.*, 2011, **83**, 205115.
7   T. Qi, I. Grinberg and A. M. Rappe, *Phys. Rev. B: Condens. Matter Mater. Phys.*, 2011, **83**, 224108.
8   I. Grinberg, W. D. Vincent, M. Torres, G. Gou, D. M. Stein, L. Wu, G. Chen, E. M. Gallo, A. R. Akbashev, P. K. Davies, J. E. Spanier and A. M. Rappe, *Nature*, 2013, **503**, 509–512.
9   W. Zhou, H. Deng, P. Yang and J. Chu, *Appl. Phys. Lett.*, 2014, **105**, 111904.
10 T. Su, H. Jiang, H. Gong and Y. Zhai, *J. Mater. Sci.*, 2010, **45**, 3778–3783.
11 S. Ramesh, B. A. Shutzberg, C. Huang and E. P. Giannelis, *IEEE Trans. Adv. Packag.*, 2003, **26**, 17–24.
12 E. Fortunato, P. Barquinha and R. Martins, *Adv. Mater.*, 2012, **24**, 2945–2986.
13 R. N. Das and V. R. Markovich, *IEEE Nanotechnol. Mag.*, 2010, **4**, 18–24.
14 S. Liu, H. Zhang, L. Sviridov, L. Huang, X. Liu, J. Samson, D. Akins, J. Li and S. O'Brien, *J. Mater. Chem.*, 2012, **22**, 21826.
15 S. Liu, L. Huang, W. Li, X. Liu, S. Jing, J. Li and S. O'Brien, *Nanoscale*, 2015, **7**, 11766.
16 L. Huang, S. Liu, B. J. Van Tassell, X. Liu, A. Byro, H. Zhang, E. S. Leland, D. L. Akin, D. A. Steingart, J. Li and S. O'Brien, *Nanoscale*, 2013, **24**, 415602.
17 B. Sundarakannan, K. Kakimoto and H. Ohsato, *J. Appl. Phys.*, 2003, **94**, 5182–5187.
18 E. M. Kopnin, S. Y. Istomin, O. G. D'yachenko, E. V. Antipov, P. Bordet, J. J. Capponi, C. Chaillout, M. Marezio, S. de Brion and B. Souletie, *Mater. Res. Bull.*, 1995, **30**, 1379–1386.
19 L. Luisman, A. Feteira and R. Klaus, *Appl. Phys. Lett.*, 2011, **99**, 192901.
20 A. M. Quittet, M. I. Bell, M. Krauzman and P. M. Raccah, *Phys. Rev. B: Solid State*, 1976, **14**, 5068–5072.
21 Z. X. Shen, Z. P. Hu, T. C. Chong, C. Y. Beh, S. H. Tang and M. H. Kuok, *Phys. Rev. B: Condens. Matter Mater. Phys.*, 1995, **52**, 3976–3980.
22 A. Bartasyte and J. Kreisel, *Appl. Phys. Lett.*, 2010, **96**, 262903.
23 P. Yang, D. Zhao, D. I. Margolese, B. F. Chmelka and G. D. Stucky, *Nature*, 1998, **396**, 152–155.
24 G. L. Brennecka, J. F. Ihlefeld, J. P. Maria, B. a. Tuttle and P. G. Clem, *J. Am. Ceram. Soc.*, 2010, **93**, 3935–3954.
25 R. W. Schwartz, *Chem. Mater.*, 1997, **4756**, 2325–2340.
26 E. Fortunato, P. Barquinha and R. Martins, *Adv. Mater.*, 2012, **24**, 2945–2986.
27 H. Sirringhaus, *Adv. Mater.*, 2005, **17**, 2411–2425.
28 D. K. Hwang, R. R. Dasari, M. Fenoll, V. Alain-Rizzo, A. Dindar, J. W. Sim, N. Deb, C. Fuentes-Hernandez, S. Barlow, D. G. Bucknall, P. Audebert, S. R. Marder and B. Kippelen, *Adv. Mater.*, 2012, **24**, 4445–4450.
29 J. Y. Kim, O. Voznyy, D. Zhitomirsky and E. H. Sargent, *Adv. Mater.*, 2013, **25**, 4986–5010.
30 C. J. Brinker and G. W. Scherer, *Sol–gel science, the physics and chemistry of sol–gel processing*, Academic Press, Boston, 1990.

31 A. P. Dunlop and F. N. Peters, *The Furans*, Reinhold Publishing Co., New York, NY, USA, 1953.

32 B. K. Kandola, J. R. Ebdon and K. P. Chowdhury, *Polymers*, 2015, **7**, 298–315.

33 P. Kim, N. M. Doss, J. P. Tillotson, P. J. Hotchkiss, P. Ming-Jen, S. R. Marder, J. Li, J. P. Calame and J. W. Perry, *ACS Nano*, 2009, **3**, 1581–2592.

34 E. H. Kerner, *Proc. Phys. Soc., London, Sect. B*, 1956, **69**, 802–807.

35 N. Jayasundere and B. V. Smith, *J. Appl. Phys.*, 1993, **73**, 2462.

36 M. G. Todd and F. G. Shi, *IEEE Trans. Dielectr. Electr. Insul.*, 2005, **12**(3), 601–611.

37 M. Ezzat, N. A. Sabiha and M. Izzularab, *Appl. Nanosci.*, 2014, **4**, 331–338.

38 I. Krad, O. Bidault, S. Said and M. El Maaoui, *Mater. Lett.*, 2015, **159**, 237–240.

39 H. Birol, D. Damjanovic and N. Setter, *J. Am. Ceram. Soc.*, 2005, **88**(7), 1754–1759.

40 G. Shirane, H. Danner, A. Pavlovic and R. Pepinsky, *Phys. Rev.*, 1954, **93**(4), 672–673.

41 H. Ge, Y. Huang, Y. Hou, H. Xiao and M. Zhu, *RSC Adv.*, 2014, **4**, 23344–23350.

42 R. H. Kulkarni and S. G. Ingle, *J. Phys. D: Appl. Phys.*, 1972, **5**, 1474–1477.

43 Y. Wang, Y. Zhigou, Y. Li, Y. Qunbao and W. Dong, *Ceram. Int.*, 2007, **33**, 1611–1615.

44 K. Kanie, Y. Numamoto, S. Tsukamoto, H. Takahashi, H. Mizutani, A. Terabe, M. Nakya, J. Tani and A. Muramatsu, *Mater. Trans., JIM*, 2011, **52**, 2119–2125.

45 J. Li, Y. Li, Z. Zhou, R. Guo and A. Bhalla, *J. Appl. Phys.*, 2014, **115**, 093104.

46 J. Li, Y. Li, Z. Zhou, R. Guo and A. Bhalla, *Ceram. Int.*, 2015, **41**(5A), 6657–6662.

47 L. Huang, Z. Chen, J. D. Wilson, S. Banerjee, R. D. Robinson, I. P. Herman, R. Laibowitz and S. O'Brien, *J. Appl. Phys.*, 2006, **100**, 034316.